


Simple method for determining metal power oxidation kinetics with a zirconia sensor

Jarrold D. Milshtein^{1,2} · Soumendra N. Basu^{1,2} · Srikanth Gopalan^{1,2} · Uday B. Pal^{1,2} 

Received: 19 March 2015 / Accepted: 29 June 2015 / Published online: 3 July 2015
© Springer Science+Business Media Dordrecht 2015

Abstract A basic zirconia oxygen sensor was utilized to monitor the gas–solid oxidation reaction characteristics of metal/metal-oxide powder beds. The method described allowed for simple determination of chemical reaction rate constants for the oxidation reactions. The signal output of the sensor was analyzed for oxidation of the powder bed and diffusion of oxygen into the powder bed. The oxygen transport mechanisms occurring inside the sensor were described to further understand the signal outputs from the powder bed, and a discussion of relevant thermodynamic and kinetic theory was provided. Two metal/metal-oxide systems were examined using this device to demonstrate its performance. The simple Ni/NiO system was chosen to demonstrate feasibility, and the complex W/WO₃ system was chosen to demonstrate versatility of the sensor. Combining the experimental data with relevant kinetic theory, chemical reaction rate constants were calculated from plots of sensor ocv versus time for each reaction step during the metal oxidation sequences.

Keywords Nickel · Tungsten · Oxidation · Oxygen sensor · Zirconia

1 Introduction

In many studies of metal oxidation reactions, thermogravimetry has been the primary method of revealing kinetic parameters of the reactions [1–3]. The authors have been involved in ongoing research to study the reduction and oxidation kinetics of tungsten powder beds by water vapor and carbon dioxide for energy applications [1, 3, 4]. In the specific case of tungsten oxidation by water vapor, it was discovered that under certain experimental conditions, tungsten metal and its oxides are highly volatile [5–7]. The initial motivation to develop a new method to monitor powder bed oxidation reactions was due to an inability to perform thermogravimetry. Tungsten volatility under water vapor would render thermogravimetric mass measurements inaccurate, as the balance cannot simultaneously account for mass changes due to oxidation reactions and volatilization. Thus, an alternative methodology for determining kinetic parameters was desired.

This study aims to demonstrate that a simple oxygen sensor can be used to determine the rates of oxidation reactions in a metal/metal-oxide powder bed, by measuring a local oxygen partial pressure (P_{O_2}) in the powder bed. This study describes the design and analysis of such a method. Relevant kinetic theory is provided, and calculations required for estimating chemical reaction rate constants from the sensor technique are described. Lastly, this study demonstrates proof of concept by providing results of experiments to monitor nickel and tungsten oxidations, as well as diffusion into a non-reacting powder bed.

2 Experimental

2.1 Sensor fabrication

Sensors were constructed using cylindrical calcia-stabilized zirconia (CaSZ) crucibles (Advalue Technology #Zc-2010),

✉ Uday B. Pal
upal@bu.edu

¹ Department of Mechanical Engineering, Boston University, 110 Cummington Street, Boston, MA 02215, USA

² Division of Materials Science and Engineering, Boston University, 15 Saint Mary's Street, Brookline, MA 02446, USA

and the crucible dimensions were as follows: 22-mm inner diameter, and 33-mm height. CaSZ was selected as a sensor material due to its low cost and availability. An approximately 2-mm diameter circle at the center of the outer bottom of the crucible was covered with an approximately 0.1-mm thick layer of platinum paste. Platinum paste was also applied to the inner bottom surface of the crucible in an approximately 5-mm diameter, 0.1-mm thick layer. The platinum paste was dried by heating the sensor in a box furnace to 1073 K (800 °C) in air for 1 h. This step also removed organic materials from the paste. The sensor was then filled with metal or metal oxide powder as described later in this section.

The sensor (CaSZ crucible) sat on a piece of 99.9 % pure, 52 mesh platinum gauze (Alfa Aesar #10283), which acted as the reference electrode current collector. A 6.35-mm outer diameter bored alumina tube threaded with platinum wire was submerged into the powder bed. The platinum wire was melted into a bead at the bottom of the alumina tube, and the bead made contact with the platinum paste at the inner bottom of the crucible, acting as the working electrode. In this design, the platinum wire of the working electrode is shielded from the metal powder by the surrounding alumina tube. Only the platinum bead at the end of the wire contacts the platinum paste that is painted at the inner bottom of the CaSZ crucible (working electrode of the sensor). Therefore, the working electrode senses only the local P_{O_2} at the crucible bottom. Thus, the sensor could be represented as a galvanic cell of the following form: $[\text{Pt}, P_{O_2}^{\text{ref}} | \text{Zirconia} | P_{O_2}, \text{Pt}]$ [8]. A schematic of the sensor design has been provided in Fig. 1a.

The sensor was sealed inside of a tube furnace as shown in Fig. 1b. The sensor and platinum mesh current collector sat directly on top of an alumina tube with a 3.18-mm inner diameter, through which all gases were introduced into the furnace. By placing the sensor's reference electrode directly on top of the gas inlet tube, the reference electrode was ensured to be the first experimental component to equilibrate. This entire experimental set-up was sealed inside a larger alumina tube, 7-cm inner diameter and 91 cm tall, oriented vertically. The larger alumina tube was sealed using custom-machined vacuum grade aluminum end caps and high-temperature silicone O-rings. Gas inlets (bottom of the tube) and outlets (top of the tube), as well as electrical leads, were sealed using Swagelok Ultra-Torr style vacuum fittings which bolted to the custom end caps. The sensor rested 45 cm up the larger alumina tube such that their position was aligned with the furnace's hot zone. During experiments, the sensor ocv was measured using either a Solartron potentiostat (model #1280B) or Fluke Hydra data logger (model #2625A).

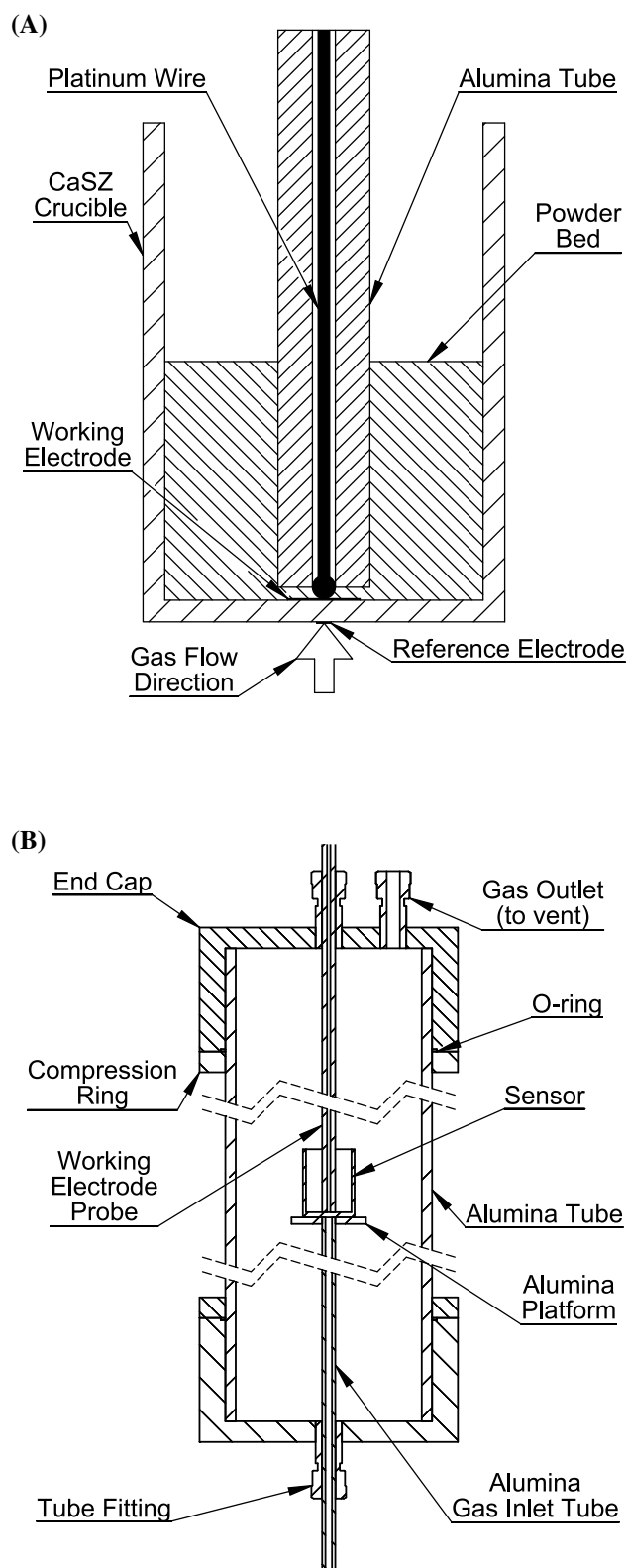


Fig. 1 Schematics of the experimental apparatus: **a** the CaSZ oxygen sensor for measuring local P_{O_2} during a metal powder oxidation reaction; **b** the CaSZ oxygen sensor sealed inside an alumina tube with vacuum grade end caps (electrical leads are not shown)

2.2 Oxidation experiments procedure

Oxidation experiments were performed by filling the CaSZ crucible sensor with either nickel or tungsten powder. In experiments in which nickel metal powder was oxidized, 1.6 g or 2.0 g of 3–7 micron, 99.9 % nickel powder (Alfa Aesar #10256) was used. In experiments in which tungsten metal powder was oxidized, 1.2, 1.6, or 2.0 g of 12 micron, 99.9 % tungsten powder (Alfa Aesar #10401) was used.

Forming gas (5 % hydrogen, 95 % argon) (Airgas #ARHY5300) was passed through the sealed alumina chamber at a rate of $2000 \text{ cm}^3 \text{ min}^{-1}$. Before entering the furnace, however, the gas mixture was purified by passing it through a calcium sulfate moisture trap. The sealed alumina chamber was purged with the forming gas for 30 min and then heated to 1123 K (850 °C) at a rate of 8.3 K min^{-1} . After the furnace had equilibrated at 1123 K (850 °C) for 1 h, ocv measurements were recorded using the Solartron potentiostat. Once the ocv signal had reached a steady state, the gas type was switched to air at a $2000 \text{ cm}^3 \text{ min}^{-1}$ flow rate. Air was passed through a calcium sulfate moisture trap before entering the furnace. ocv measurements were recorded until the ocv returned to a value of 0 V. The oxidizing gas flow was turned off, and the experimental set-up was allowed to cool in air. The furnace was cooled at a rate of 8.3 K min^{-1} .

2.3 Gas diffusion experiments procedure

Gas diffusion into a powder bed of tungsten trioxide contained in the CaSZ crucible sensor was studied using 3.0 g of 10–20 micron, 99.8 % tungsten trioxide powder (Alfa Aesar #11828). A mixture of 5 % oxygen and 95 % argon (Airgas #XO2AR95C3005000) (pre-cleaned by passing through a calcium sulfate moisture trap) was passed through the sealed alumina chamber at a rate of $2000 \text{ cm}^3 \text{ min}^{-1}$. The sealed alumina chamber was purged using this gas type and flow rate for 30 min and then heated to 1123 K (850 °C) at a rate of 8.3 K min^{-1} . The furnace was allowed to equilibrate at 1123 K (850 °C) for 1 h. Then, the gas type was switched to dry air, and ocv measurements were recorded using the Fluke Hydra data logger until the ocv returned to a value of 0 V. The gas flow was turned off and the experimental set-up cooled in air. The furnace was cooled at a rate of 8.3 K min^{-1} .

3 Theory

3.1 Electroceramics

Zirconium dioxide (ZrO_2 or zirconia) is a well-known oxygen anion conductor, and calcia (CaO) dopant, such as

in CaSZ, increases the oxygen anion conductivity [9]. An oxygen concentration gradient across the zirconia induces an electromotive force (emf) which can be described by the Nernst equation, shown in Eq. (1) [8]. In Eq. (1), E is the emf, R is the gas constant, T is absolute temperature, F is Faraday's constant, $P_{\text{O}_2}^{\text{ref}}$ is a known reference oxygen partial pressure, and P_{O_2} is the unknown oxygen partial pressure being measured.

$$E = \frac{RT}{4F} \ln \frac{P_{\text{O}_2}}{P_{\text{O}_2}^{\text{ref}}} \quad (1)$$

By fixing the oxygen partial pressure at a reference electrode, $P_{\text{O}_2}^{\text{ref}}$, the unknown P_{O_2} at a working electrode can be determined by measuring the open circuit voltage (ocv) across the zirconia, assuming a negligibly small electronic leak at the experimental temperature and gas atmosphere. The electronic transference number, t_e , at 1123 K (850 °C) and $P_{\text{O}_2} \approx 10^{-21}$ atm (lowest P_{O_2} introduced through the forming gas) is $\sim 2 \times 10^{-4}$ [10]. The changing P_{O_2} at the working electrode can therefore be monitored by measuring the ocv as a function of time.

3.2 Diffusion in a finite domain

The diffusion of oxygen into a non-reacting porous powder bed can be described mathematically by considering the diffusion process in a finite slab. The relevant solution to the diffusion equation for a fixed oxygen concentration at the powder bed interface and a changing oxygen concentration gradient inside the powder bed is given by a widely recognized series summation [11, 12]. The series summation solution to the diffusion equation could be used to model the diffusion process.

3.2.1 Thermodynamics of metal oxidation reactions

In this proof of concept study, the nickel and tungsten oxidation systems were selected for evaluating the technique. The nickel/nickel-oxide system is known to have two stable species at elevated temperatures, Ni and NiO. The nickel oxidation system was used to demonstrate the sensor's signal response to a single oxidation reaction system. The phase diagram in Fig. 2 demonstrates which phases are stable as a function of P_{O_2} and temperature.

During the full oxidation of W to WO_3 , the oxidation reaction is accepted to take place as follows: $\text{W} \rightarrow \text{WO}_2 \rightarrow \text{WO}_{2.72} \rightarrow \text{WO}_{2.96} \rightarrow \text{WO}_3$ [1–3]. The tungsten/tungsten-oxide system was selected to show how the oxygen sensor technique can be applied to this complex metal/metal-oxide system of interest for energy storage applications. The stable tungsten species are shown in the phase diagram in Fig. 3.

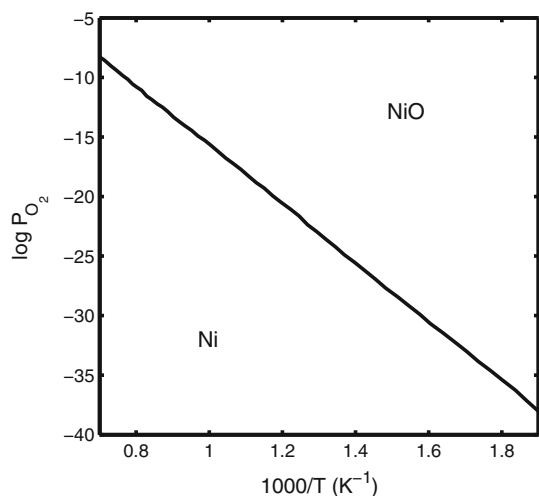


Fig. 2 Phase stability diagram of the Ni–O system as a function of P_{O_2} and temperature [13–15]

Phase diagrams were generated by HSC chemistry [13]. Data for nickel and tungsten metals were reported by NASA [14]. Data on tungsten oxides were reported by Barin [15]. Nickel oxide data were reported by Barin and Scientific Group Thermodata Europe [15, 16].

3.2.2 Moving front reaction kinetics

In a chemical reaction between a gas, $A_{(g)}$, and a loosely packed, powdered solid, $B_{(s)}$, the chemical reaction can be generically described as follows:



In a fixed and isothermal powder bed, the reaction can take place as a moving front when the chemical reaction rate is

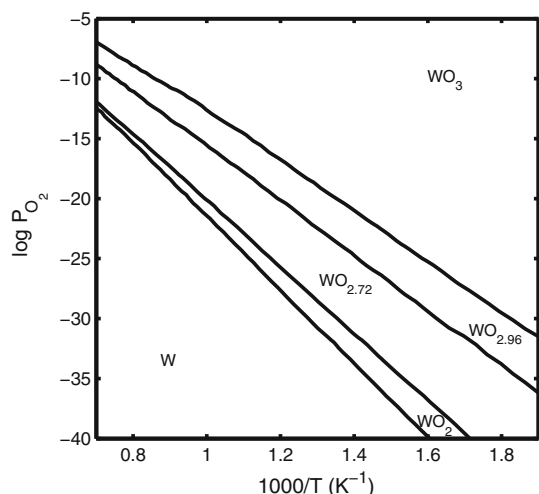


Fig. 3 Phase stability diagram of the W–O system as a function of P_{O_2} and temperature [13, 15, 16]

slower than the gas diffusion rate. As the gas–solid reaction begins, a thin layer of solid product $F_{(s)}$ forms in place of reactant $B_{(s)}$. The layer of solid product is also a porous powder. Due to the porous nature of the powder layer, reactant gas $A_{(g)}$ diffuses through the $F_{(s)}$ powder layer to the new interface between reactant $B_{(s)}$ and product $F_{(s)}$. The reactant gas $A_{(g)}$ then continues to react with reactant powder $B_{(s)}$ to form additional product $F_{(s)}$. Four assumptions are made in the description of gas–solid moving front reaction where the solid is a powder [1–3]:

1. The reaction front maintains planar geometry as it moves through the powder bed.
2. The densities of the solid product $F_{(s)}$ and solid reactant $B_{(s)}$ are much greater than the density of the reactant gas $A_{(g)}$. Also, the densities of the two solid phases ($F_{(s)}$ and $B_{(s)}$) are assumed to be of the same order of magnitude.
3. The reaction front moves at a rate small in comparison to the gas diffusion of $A_{(g)}$ through the gaseous boundary layer and into the powder bed.
4. Diffusion of product gas $E_{(g)}$ out of the powder bed is rapid and not rate controlling either.

In the oxidation reactions considered in this work, no product gas, $E_{(g)}$, was formed. Figure 4 shows a schematic of a moving front reaction, where the moving front maintains planar geometry, replacing reactant $B_{(s)}$ with product $F_{(s)}$ behind the reaction front.

The rate of reactant gas consumption in a generic gas–solid reaction can be described as a function of three kinetic resistances: reactant gas diffusion through the gaseous boundary layer, reactant gas diffusion through the solid product, and the chemical reaction rate constant

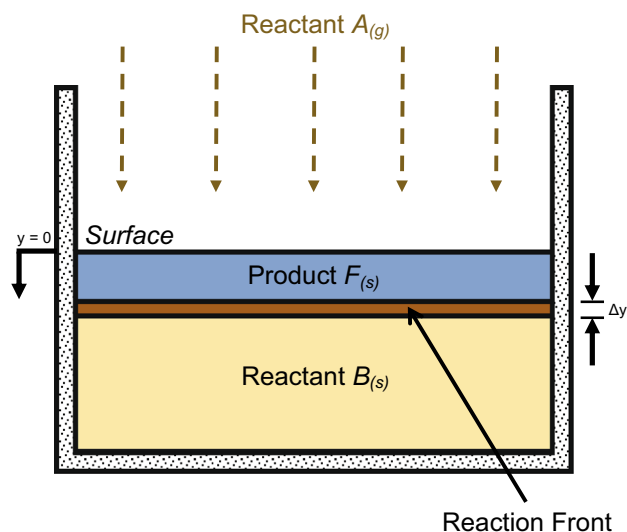


Fig. 4 Schematic of a moving front oxidation reaction (adapted from [1, 2])

[1–3, 17]. By comparing the relative magnitudes of the resistive components, it is possible to determine the rate limiting step of the gas–solid reaction.

In situations where one segment of the reaction is much more resistive than the other two, the rate of the reaction will be controlled by the most resistive segment. In this study, because the solid was a powder and reactant gases were introduced at high velocities, reactions were chemical reaction rate controlled; the rates of diffusion of $A_{(g)}$ through the gaseous boundary layer and through the solid were much greater than the chemical reaction rate. Further, under the experimental conditions, the driving force for the reaction is much greater than the activation energy required for nucleation. Thus, the oxidation reactions were kinetically driven and controlled by growth. Equation (3) shows the rate of consumption of $A_{(g)}$ assuming a chemical reaction rate control, where S is the surface area of the planar moving front, dN_A/dt is the molar rate of consumption of $A_{(g)}$, C_A is the concentration of $A_{(g)}$ outside the powder bed, and k'' is the reaction rate constant [17].

$$\frac{-1}{S} \times \frac{dN_A}{dt} = C_A k'' \tag{3}$$

By rearranging Eq. (3) and substituting for well-known terms, it is possible to define the mass rate of consumption of reactant solid $B_{(s)}$ as shown in Eq. (4), where b is the stoichiometric coefficient of reactant $B_{(s)}$, M_B is the molar mass of reactant $B_{(s)}$, P_A is the partial pressure of reactant gas $A_{(g)}$, R is the gas constant, T is absolute temperature, k_0 is a rate constant, Q is the activation energy of the reaction, and dm_B/dt is the mass rate of consumption of reactant $B_{(s)}$ [1, 2].

$$\frac{dm_B}{dt} = -SM_B b k_0 \frac{P_A}{RT} \exp\left(\frac{-Q}{RT}\right) \tag{4}$$

From Eq. (4), it can be concluded that for a fixed partial pressure of reactant gas $A_{(g)}$ and fixed temperature, the velocity of the moving reaction front is a constant. In order to show this conclusion mathematically, the mass rate of consumption of $B_{(s)}$ must be related to the position of the reaction front as shown in Eq. (5), where ρ_B is the density of reactant $B_{(s)}$, ϕ_B is the porosity of the powder bed, and dy/dt is the velocity of the moving front.

$$\frac{dy}{dt} = \frac{-1}{\rho_B(1 - \phi_B)} M_B b k_0 \frac{P_A}{RT} \exp\left(\frac{-Q}{RT}\right) \tag{5}$$

The velocity of the reaction front is independent of the moving front surface area and of the instantaneous position of the reaction front in the powder bed. In other words, for a given P_A , T , and ϕ_B , the reaction time will increase linearly with powder height, and if the moving front surface area is constant, it will also scale linearly with the mass of the powder bed.

3.2.3 Bulk reaction behavior

In comparison to the moving front mechanism, when the rate of gas diffusion into a reacting powder bed is even greater in comparison to the chemical reaction rate, the reaction can be characterized by bulk reaction behavior. In this case, the reactant gas first surrounds each powder particle throughout the bed. Next, each powder particle is believed to react simultaneously according to the shrinking core model. A solid layer of product $F_{(s)}$ forms on the surface of a particle of reactant $B_{(s)}$, and the reacting interface moves radially into the solid particle. Finally, a solid particle comprised entirely solid product $F_{(s)}$ remains [17]. Figure 5 shows a schematic of such a bulk reaction, where each powder particle reacts simultaneously according to the shrinking core model.

If the diffusion through the product layer $F_{(s)}$ is faster than the chemical reaction rate, the total time of this reaction can be described as shown in Eq. (6), where ρ_B is the density of solid B, r_i is the mean initial radius of solid B particles, and τ is the total time required for the bulk reaction to take place [17].

$$\tau = \frac{\rho_B r_i RT}{b k'' P_A} \tag{6}$$

4 Calculations

If the oxidation reactions are chemical reaction rate controlled, determining the numeric value for the chemical reaction rate, k'' , becomes relatively simple. For the moving front reaction, Eq. (4) must first be integrated as a

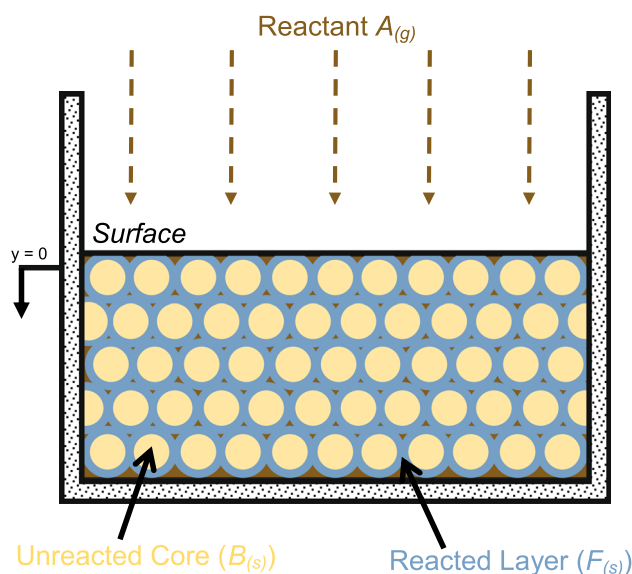


Fig. 5 Schematic of a bulk oxidation reaction

function of time and rearranged to Eq. (7), where τ is the total reaction time, and m_B^i is a constant of integration equivalent to the initial mass of solid reactant $B_{(s)}$.

$$k'' = \frac{m_B^i RT}{SM_B b P_A \tau} \quad (7)$$

The total time of a given reaction can be determined by analyzing the numerical second derivative of the sensor's voltage output; the start and finish times of a reaction can be identified using the data features described in the Sect. 5 of this paper.

To solve for the chemical reaction rate of a bulk reaction, Eq. (6) can be easily manipulated into Eq. (8).

$$k'' = \frac{\rho_B r_i RT}{b \tau P_A} \quad (8)$$

5 Results and discussion

5.1 Identifying reaction behaviors

5.1.1 Moving front oxidation response

Figure 6 demonstrates the anticipated sensor response to a single moving front oxidation reaction. The moving front oxidation will begin at the top of the powder bed once the appropriate P_{O_2} corresponding to the oxidation reaction has been reached. Due to the high velocity of the gas introduced around the sensor, the top of the powder bed should begin reacting almost immediately after the oxidizing gas is introduced. As the reaction front moves down the powder bed, the P_{O_2} of the reaction front will be fixed. The

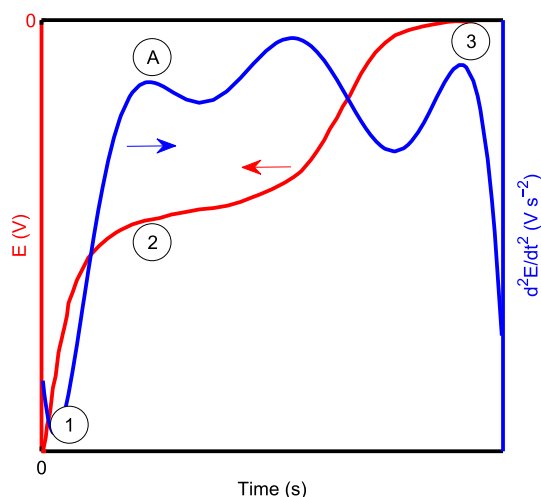


Fig. 6 Anticipated time versus ocv and time versus d^2E/dt^2 curve from the sensor response during a single moving front oxidation reaction

concentration gradient between the moving front and the working electrode will decrease as oxygen diffuses toward the bottom of the powder bed and as the front approaches the bottom of the powder bed. Consequently, the P_{O_2} at the bottom of the powder bed will increase as the oxidation moving front approaches the bottom of the powder bed. When the front reaches the bottom of the sensor, the P_{O_2} at the working electrode will be instantaneously fixed due to the oxidation reaction taking place. The sensor response to a moving front reaction is demonstrated by the regime between Point 1 and Point 2 in Fig. 6. This regime is expected to exhibit a decreasing slope.

Since the time versus ocv curve changes rapidly when the moving front oxidation reaction reaches the working electrode, the end of a moving front oxidation reaction is best indicated by locating the first maxima in the second derivative of the sensor output, as indicated by Point A in Fig. 6. In order to appropriately describe the transient sensor behavior, a solution to the diffusion equation across a finite distance with a moving boundary must be derived. However, such a governing equation to describe the transient ocv response of the sensor during the oxidation process is not necessary since the goal of the experiments was to determine only the total reaction time.

After the moving front reaction has completed, oxygen gas will continue to diffuse into the powder bed until the P_{O_2} inside the powder bed equilibrates with the P_{O_2} at the reference electrode. The measured P_{O_2} at the working electrode can therefore be described in terms of oxygen diffusion through a powder bed of fixed height exposed to a fixed P_{O_2} at the surface. The sensor response to this diffusion process is shown between Point 2 and Point 3 in Fig. 6.

Moving front reactions can also be identified by comparing ocv curves from reacting powder beds of different total bed heights. According to Eq. (5), if the velocity of the reaction front is constant, total reaction times will scale with bed height.

5.1.2 Bulk oxidation response

For a single bulk oxidation reaction, powder particles react according to the shrinking core model, and the ocv produced by the sensor will be determined by the P_{O_2} of the gas phase surrounding powder particles at the working electrode. For sufficiently small bed heights, however, this diffusion can be considered rapid compared to the time scale of the bulk reaction. When there is no more oxygen consumption, the rate of increase of ocv will increase due to oxygen gas diffusion.

Critically, for small bed heights, the total time required for a bulk oxidation reaction to take place depends on powder particle size, not the total powder bed mass. Thus,

by reacting two powder beds comprised particles of the same size but different total powder bed masses, bulk reactions can be identified. If the total time of the reaction is independent of total powder bed mass, the reaction is indeed a bulk reaction. This directly contrasts moving front reaction behavior where the total time of the reaction does depend on the total mass of the powder bed.

5.1.3 Gas diffusion

After oxidation reactions are complete inside the sensor, oxygen transport will be entirely diffusion controlled, as no oxidation reaction will fix the P_{O_2} in the powder bed. The measured P_{O_2} at the working electrode as a function of time can therefore be described as a diffusion process occurring through a finite slab, where the P_{O_2} of the surface is fixed by the P_{O_2} of the gas–powder interface. The diffusion length is fixed by the height of the powder bed. Given the described diffusion boundary conditions, the sensor response to diffusion can be described by the ocv induced due to a time-varying oxygen concentration at the bottom of the powder bed. The anticipated sensor response to the diffusion process is depicted between Point 2 and Point 3 in Fig. 6.

5.2 Experimental results

5.2.1 Nickel oxidation

Results from oxidation experiments of 1.6 and 2.0 g of nickel are shown in Figs. 7 and 8, respectively. The approximate second derivatives shown in these figures were calculated by first fitting a high-order polynomial to the data in the time range of interest. In the case of the 1.6 g oxidation, a 7th order polynomial was used, and in the case of the 2.0 g oxidation, a 9th order polynomial was used. The second derivatives of these polynomials were used as the approximate second derivatives of the data to produce smooth second derivative curves. The polynomial fits are also included in Figs. 7 and 8.

The sensor outputs due to these oxidations closely match the anticipated behavior described for Fig. 6. The moving front reaction is characterized by an increasing P_{O_2} with time at the working electrode, with a decreasing slope. The end of the moving front reaction is indicated by Point A on the plot of d^2E/dt^2 in Figs. 7 and 8. Then, oxygen continues to diffuse into the powder bed until equilibrium is achieved. To locate the various regimes in Figs. 7 and 8, refer to the numbering system described previously in the Sect. 5.1.1

Notably, in the case of the 2.0 g powder bed (Fig. 8), the theoretical sensor ocv is -1.13 V under the described experimental condition, which is close the measured ocv

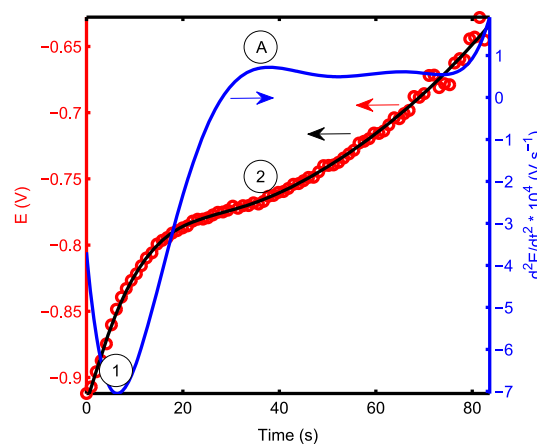


Fig. 7 Sensor response curve to oxidation of 1.6 g of nickel. Experimental data (open red circles) is plotted along with a polynomial fit (solid black line) and approximate second derivative (solid blue line) of the data

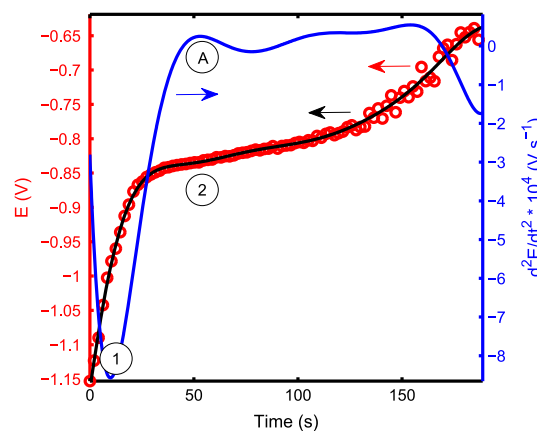


Fig. 8 Sensor response curve to oxidation of 2.0 g of nickel. Experimental data (open red circles) is plotted along with a polynomial fit (solid black line) and approximate second derivative (solid blue line) of the data

(-1.15 V) at $t = 0$ s. $t = 0$ s was defined as the time at which the reference electrode equilibrated. When comparing Figs. 7 and 8, however, it is evident that the ocv values measured at $t = 0$ s were different for the 1.6 and 2.0 g nickel powder oxidation experiments. This difference can be explained. During the time in which it takes the reference electrode to equilibrate, oxygen gas can leak (diffuse) into the powder bed. If the powder bed height is sufficiently small, the oxygen leak to the working electrode will be large, causing the magnitude of the ocv to decrease relative to the theoretical ocv value at $t = 0$. This behavior was observed in the case of the 1.6 g nickel powder bed (Fig. 7). In contrast, if the powder bed height is sufficiently large, only a negligible amount of oxygen will reach the working electrode during the reference electrode equilibration time, and the measured ocv will be equal to the

theoretical value. This behavior was observed in the case of the 2.0 g nickel powder bed (Fig. 8). Thus, the sensor performance improved when the powder bed height was increased. However, since the reference electrode equilibration time was small compared to the total time scale of the oxidation reaction, the small error associated with oxygen leak into the powder bed is not believed to affect the kinetic analysis. Additionally, as long as the gas phase P_{O_2} at the working electrode is below the equilibrium P_{O_2} for the oxidation reaction, the oxygen leak will not affect the reaction mechanisms previously described.

The rate at which the moving fronts proceed down the powder bed should be the same in both nickel oxidation experiments. Since the same powder and the same experimental conditions were used in both the 1.6 and 2.0 g oxidation experiments, the chemical reaction rates should also be the same in both experiments. Thus, by calculating the chemical reaction rates for both experiments by using Eq. (7), the moving front behavior can be quantitatively confirmed. The compiled values of variables needed to solve for the chemical reaction rate constant are provided in Table 1. By substituting these values into Eq. (7), the chemical reaction rate constant can be solved.

For the oxidation of 1.6 g of nickel, $k'' = 0.47 \text{ m s}^{-1}$, and for the oxidation of 2.0 g of nickel, $k'' = 0.44 \text{ m s}^{-1}$. Between the two experiments, the calculated chemical reaction rate constants differed by 6.8 %. The nickel oxidation occurs essentially by a moving front mechanism. The similarity of reaction rates further implies that the velocities of the moving fronts in both nickel oxidation experiments were also similar (Eq. 5), and as can be seen from the data in Table 1, the time scales of the reactions were approximately proportional to bed heights (or masses since the crucible used had a fixed surface area). The equality of moving front velocities with different reaction time scales agrees with the description of a moving front reaction.

The experimental results provided in Figs. 7 and 8 show only the times during experiments where moving front oxidation occurs. Figure 9 shows the entire ocv curve for the 1.6 g of nickel oxidation, including the regime corresponding to gas diffusion into the powder bed after the moving front reaction ceases.

Results from a diffusion-only experiment are shown in Fig. 10 in which oxygen diffused into a non-reacting WO_3 powder bed. Initially, the oxygen partial pressure was $P_{O_2} = 0.05 \text{ atm}$, which is a greater P_{O_2} than the $WO_{2.96}/WO_3$ equilibrium P_{O_2} at 1123 K (850°C). The high P_{O_2} implies that reduction of the WO_3 to any lower oxide would not occur; the powder bed remained as WO_3 for the entire experiment. Since the powder bed remained intact during the experiment and no chemical reaction occurred,

Table 1 Chemical reaction rate analysis for nickel oxidation

Variable	Value (SI units)	
M_B^1	0.001606 kg	0.002051 kg
S	$3.485 \times 10^{-4} \text{ m}^2$	$3.485 \times 10^{-4} \text{ m}^2$
M_B	$0.05869 \text{ kg mol}^{-1}$	$0.05869 \text{ kg mol}^{-1}$
b	2	2
P_A	$2.128 \times 10^4 \text{ Pa}$	$2.128 \times 10^4 \text{ Pa}$
τ	37 s	53 s
T	1123 K	1123 K
R	$8.314 \text{ J mol}^{-1} \text{ K}^{-1}$	$8.314 \text{ J mol}^{-1} \text{ K}^{-1}$
k''	0.47 m s^{-1}	0.44 m s^{-1}

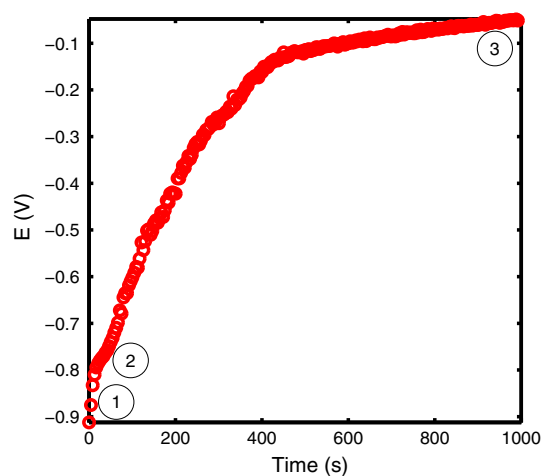


Fig. 9 Sensor response curve to oxidation of 1.6 g of nickel. Full time scale of experiment is depicted

the sensor signal output can be completely described by oxygen diffusion in a porous, finite media. The ocv curve from the gas diffusion experiment into a non-reacting, porous powder bed closely matches the behavior depicted between Points 2 and 3 in Fig. 9 after the $Ni \rightarrow NiO$ oxidation reaction had occurred. Thus, the ocv curve behavior after the oxidation reaction is believed to be entirely controlled by diffusion of oxygen into the porous powder bed.

5.2.2 Tungsten oxidation

Results from an experiment in which 2.0 g of tungsten was oxidized are provided in Fig. 11. Experimental results from the tungsten oxidation experiment were much more complex than the results of the nickel oxidation. The tungsten oxidation is best characterized by combining the bulk reaction, moving front reaction, and diffusion behaviors previously discussed. Importantly, it was assumed that reactant gas diffusion into the powder bed is fast (true for

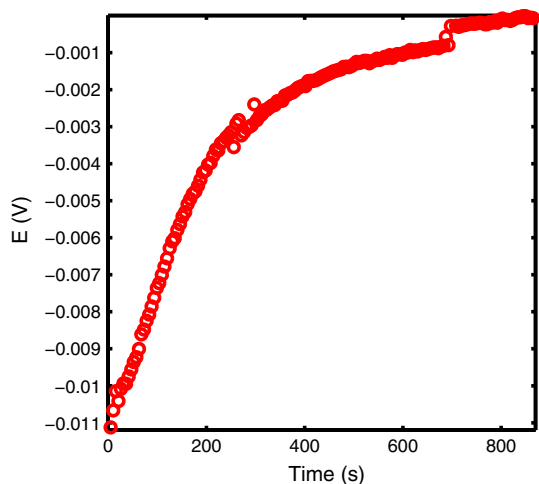


Fig. 10 Sensor response curve to diffusion into a non-reacting powder bed

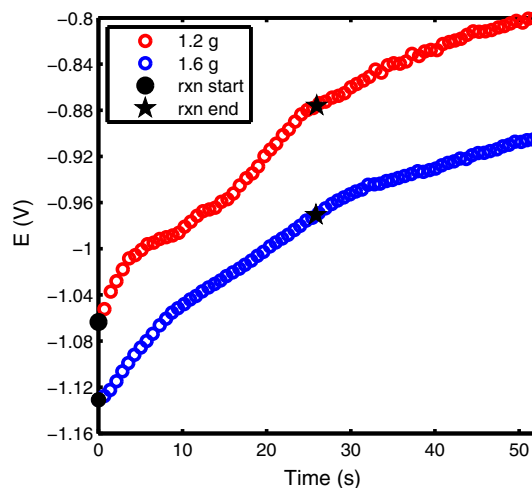


Fig. 12 Comparison of $W \rightarrow WO_2$ reactions during 1.2 and 1.6 g tungsten oxidation experiments

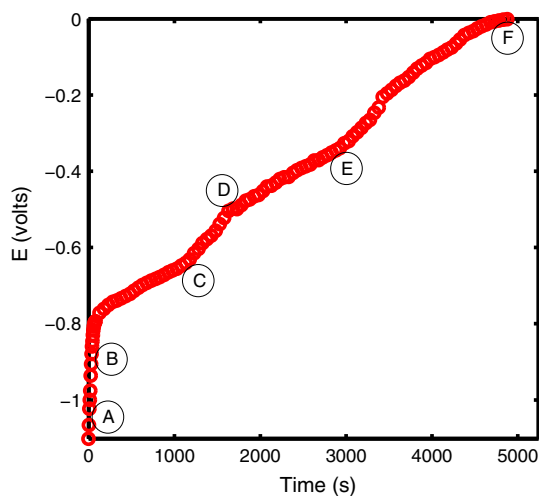


Fig. 11 Sensor response curve to oxidation of 2.0 g of tungsten

relatively shallow beds), and thus, there is no concentration gradient of the gas phase in the powder bed above the reaction front. As the powder bed height increases, a gas phase concentration gradient is expected to develop, which may result in multiple reaction fronts. If the powder bed was taller, multiple reaction fronts would exist in the powder bed, and a more complicated analysis would be required to distinguish the kinetic rates of each individual reaction.

The time versus ocv curve in Fig. 11 is first characterized by a region of steep slope, presented from Point A to Point B. This region corresponds to the bulk oxidation reaction, $W \rightarrow WO_2$. As previously described in the Sect. 5.1.2, the slope of the ocv versus time curve between Point A and Point B in Fig. 11 decreases near Point B because the $W \rightarrow WO_2$ reaction is followed by the $WO_2 \rightarrow WO_{2.72}$ (Point B to Point C) moving front reaction.

By closely analyzing the first few seconds of ocv curves from tungsten oxidation experiments, the bulk reaction behavior can be confirmed. Figure 12 compares ocv curves from tungsten oxidations with 1.2 and 1.6 g of tungsten powder. Circles represent the beginning of the $W \rightarrow WO_2$ reactions, and stars represent the ends of the reactions (rxn). The experiments represent two oxidations with different powder bed heights, and the regimes of steep slope indicate that reaction time did not scale with powder bed height. The reaction times were the same. Thus, it is believed that the first 26 s of tungsten oxidation can be described as a bulk $W \rightarrow WO_2$ reaction. Again, the initial ocv values vary between the two experiments due to the different diffusion gradients prior to introducing the oxidizing gas.

After the $W \rightarrow WO_2$ (Point A to Point B) reaction, the ocv curve shown in Fig. 11 quickly decreases in slope indicating a moving front reaction, corresponding to the $WO_2 \rightarrow WO_{2.72}$ (Point B to Point C) oxidation reaction. The slope then changes again and begins to decrease, indicating the moving front reaction corresponding to $WO_{2.72} \rightarrow WO_{2.96}$ (Point C to Point D) oxidation. Then, there is a third region of decreasing slope corresponding to the $WO_{2.96} \rightarrow WO_3$ (Point D to Point E) moving front reaction. Finally, the remaining portion of the curve (Point E to Point F) corresponds to gas diffusion into the powder bed as the system reaches equilibrium. Thus, the tungsten oxidation response is best represented by a combination of the three kinetic processes described in this paper: bulk oxidation, moving front oxidation, and diffusion into a non-reacting powder bed.

Calculations of chemical reaction rates from moving front reactions have already been described in the discussion of the nickel oxidation experiments. Results from tungsten oxidation experiments will be used to demonstrate

Table 2 Chemical reaction rate analysis for the $W \rightarrow WO_2$ reaction

Variable	Value (SI units)
ρ_B	19,250 kg m ⁻³
r_i	12×10^{-6} m ²
b	1
P_A	2.128×10^4 Pa
τ	26 s
T	1123 K
R	8.314 J mol ⁻¹ K ⁻¹
k''	4.1×10^{-3} m s ⁻¹

the calculation of chemical reaction rates from bulk reactions. From Fig. 12, it can be seen that the $W \rightarrow WO_2$ reaction requires 26 s to complete. The chemical reaction rate was calculated to be $k'' = 4.1 \times 10^{-3}$ m s⁻¹ using Eq. (8). Relevant values for variables necessary to calculate the chemical reaction rate are provided in Table 2.

6 Conclusion

An oxygen sensor was designed such that the P_{O_2} could be monitored within a reacting metal/metal-oxide powder bed. The sensor response displayed electronic signals corresponding to bulk and moving front oxidation reactions, as well as diffusion into a non-reacting powder bed. This device offers an alternative method to studying reaction characteristics associated with powder bed oxidation without using thermogravimetry.

To demonstrate the sensor's operation, experiments were performed to show the sensor's applicability in studying nickel and tungsten oxidation. The oxidation studies allowed for simple confirmation of the relationship between the changing P_{O_2} in the powder bed and the sensor output. The presence of moving front reactions and bulk reactions were also confirmed by studying nickel and tungsten oxidations, respectively, with different bed heights. The tungsten oxidation shows that the sensor can be used to study oxidations of complex metal/metal-oxide systems.

Acknowledgments The financial support of the Boston University Ignition Award is gratefully acknowledged. The assistance of Dr. Eric

Gratz, Mr. Romain Haboury, and Mr. Robert Sjoström is also greatly appreciated.

References

- Haboury R, Pal UB, Zink PA et al (2012) Study of an energy storage and recovery concept based on the W/WO_3 redox reaction: part I. Kinetic study and modeling of the WO_3 reduction process for energy storage. *Metall Mater Trans B* 43:1001–1010. doi:10.1007/s11663-012-9656-0
- Bustnes JA, Sichen D, Seetharaman S (1993) Application of a nonisothermal thermogravimetric method to the kinetic study of the reduction of metallic oxides: part II. A theoretical treatment of powder bed reduction. *Metall Mater Trans B* 24B:475–480
- Milshstein JD, Gergel DR, Basu SN et al (2015) Mixed ionic electronic conducting powder bed for grid level energy storage and release: a study of tungsten oxide reduction kinetics. *Int J Hydrog Energy* 40:3624–3632. doi:10.1016/j.ijhydene.2015.01.077
- Milshstein JD, Gratz E, Basu SN et al (2013) Study of the two-step W/WO_3 solar to fuel conversion cycle for syngas production. *J Power Sources* 236:95–102. doi:10.1016/j.jpowsour.2013.02.038
- Belton GR, McCarron R (1964) The volatilization of tungsten in the presence of water vapor. *J Phys Chem* 33:1852–1856
- Greene G, Finfrock C (2001) Vaporization of tungsten in flowing steam at high temperatures. *Exp Therm fluid Sci* 25:87–99
- Lassner E, Schubert WD (1999) Tungsten: properties, chemistry, technology of the element, alloys, and chemical compounds. Springer, Heidelberg, p 422
- Luo Z, Xiao J, Xia F (2006) Preparation and analysis of zirconia oxygen sensors. *Trans Nonferrous Met Soc China* 16:s82–s87
- Krishnan A (2006) Solid oxide membrane process for the direct reduction of magnesium from magnesium oxide, p 153
- Park J, Blumenthal RN (1989) Electronic transport in 8 mole percent. *J Electrochem Soc* 136:2867–2876
- Balluffi RW, Allen SM, Carter WC (2005) Chemistry, technology of the element. Wiley, New York, pp 107–109
- Pawel R (1974) Diffusion in a finite system with a moving boundary. *J Nucl Mater* 49:281–290
- Roine A (2002) HSC chemistry, 5.11 ed. Outokumpu Research Oy, Pori
- McBride BJ, Gordon S, Reno MA (1993) Thermodynamic data for fifty reference elements. NASA-TP-3287, N93-19977
- Barin I (1993) Thermodynamic data of pure substances. VCH Verlagsgesellschaft mbH, Weinheim
- Scientific Group Thermodata Europe (1999) Grenoble Campus, 1001 Avenue Centrale, BP 66. F-38402 Saint Martin d'Hères
- Levenspiel O (1999) Chemical reaction engineering, 3rd edn. Wiley, New York, pp 566–586